ARTICLE OPEN

Parallel tomography of quantum non-demolition measurements in multi-qubit devices

L. Pereira [ID][1 ✉], J. J. García-Ripoll[1 ✉] and T. Ramos [ID][1 ✉]

An efficient characterization of QND measurements is an important ingredient toward certifying and improving the performance and scalability of quantum processors. In this work, we introduce a parallel tomography of QND measurements that addresses single- and two-qubit readout on a multi-qubit quantum processor. We provide an experimental demonstration of the tomographic protocol on a 7-qubit IBM-Q device, characterizing the quality of conventional qubit readout as well as generalized measurements such as parity or measurement-and-reset schemes. Our protocol reconstructs the Choi matrices of the measurement processes, extracts relevant quantifiers—fidelity, QNDness, destructiveness—and identifies sources of errors that limit the performance of the device for repeated QND measurements. We also show how to quantify measurement crosstalk and use it to certify the quality of simultaneous readout on multiple qubits.

INTRODUCTION

Quantum non-demolition (QND) measurements allow the repeated evaluation of an observable without changing its expected value[1,2]. They have been implemented in many quantum platforms such as atomic[3–8] or solid-state systems[9–14]. In superconducting quantum processors, in particular, the most widespread qubit measurement is, in its ideal form, also a QND measurement[15–17]. In practice, this qubit readout is not yet perfectly QND and has larger errors than single- and two-qubit gates[18,19]. The origin of these measurement errors is diverse: non-dispersive interactions[20,21], leakage to excited states[22,23], decoherence[17,24], or crosstalk[25,26], and they accumulate exponentially with repeated measurements.

While state-of-the-art is adequate for restricted models of computation—e.g., variational quantum algorithms[27,28] or proof-of-principle quantum error correction[18,29,30]—large-scale and fault-tolerant quantum computing schemes[31–35] require that we improve on the quality of QND measurements, through efficient, reliable, and self-consistent characterization techniques, which also help us identify and mitigate experimental errors[36].

Quantum tomography (QT) is a powerful and general technique to characterize the evolution of a physical system[37], used e.g. in superconducting qubits[38–40], trapped ions[41–43], or photonic systems[44–46]. We proposed QND measurement tomography (QND-MT)[47] as a self-consistent reconstruction of the Choi operators for a general QND detector, describing the measurement process, its dynamics, relevant quantifiers, and sources of error. A similar approach based on gate set tomography (GST) has also been recently developed[48]. QND-MT is more informationally complete than a direct estimation of readout fidelity and QNDness[15,49,50], or a standard measurement tomography (MT)[26,51–53] of the positive operator-valued measurements (POVM).

In this work, we experimentally implement an efficient parallel QND-MT to characterize the most important measurement properties of a 7-qubit IBM-Q quantum computer[19]. The protocol exploits the low correlations between the qubit readout to implement a cheap parallel single-qubit characterization of each measurement, obtaining relevant quantifiers from the Choi

operators such as readout fidelity, QNDness, and destructiveness[47]. We observe that the device is optimized to maximize the fidelity—calibrated at around ~98% for every qubit—but not the QNDness, which varies more across the devices and it is lower on average ~96.7%. QND-MT also reveals that bit-flip errors are the main source of imperfections. Using a two-qubit QND-MT we quantify measurement crosstalk across devices. We find a similar correlation strength between local and non-local pairs of qubits, which introduces an error of less than 1% in the simultaneous execution of qubit readout. This validates the application in parallel with the single- and two-qubit tomographic protocol on the IBM-Q device, which can be executed with a constant number of circuits, avoiding the exponential scaling of a full QT. This parallelization is also extended to the post-processing of data on classical computers.
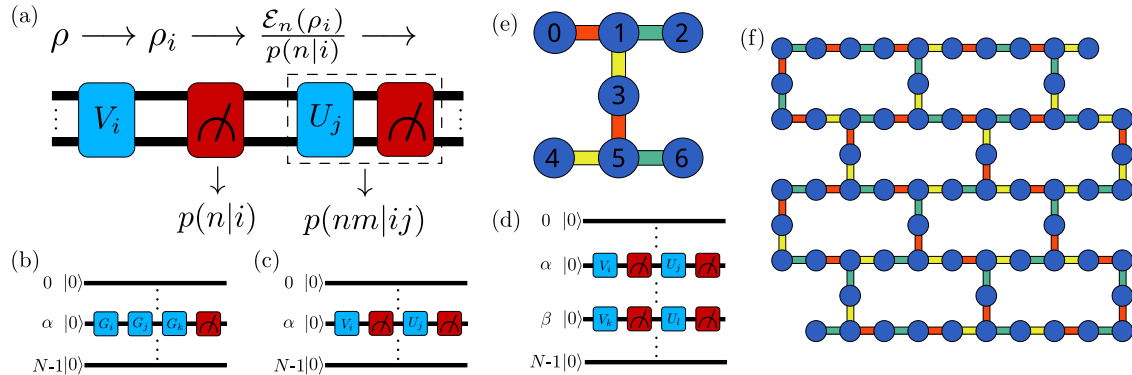
Finally, we demonstrate the generality of QND-MT by reconstructing composite measurement processes relevant to quantum error correction protocols such as parity measurements (PMs) and measurement-and-reset schemes with classical feedback. Our experiment shows that the PM involves more errors—mainly non-dispersive—than a direct QND measurement due to the presence of an entangling gate. In addition, we observe that the measurement-and-reset scheme can enhance the QND nature of the readout.

RESULTS

QND measurement tomography on a multi-qubit device

A generalized quantum measurement of an N-qubit system in state ρ is described by a set of non-trace-preserving quantum processes $\mathcal{E}_n$, which add up to a trace-preserving one, $\mathcal{E} = \sum_n \mathcal{E}_n^2$. Each individual process determines a post-measurement state $\rho_n = \mathcal{E}_n(\rho)/p(n)$, conditioned to the measurement outcome occurring with probability $p(n) = \text{Tr}(\mathcal{E}_n(\rho))$. A representation of quantum processes commonly used in QT is the Choi matrices[54]. In this representation, a measurement is described by a set of Choi

[1]Instituto de Física Fundamental IFF-CSIC, Calle Serrano 113b, Madrid 28006, Spain. ✉email: luciano.ivan@iff.csic.es; jj.garcia.ripoll@csic.es; t.ramos@csic.es

Fig. 1 Quantum circuits and parallelization strategies in the QND measurement tomography. Quantum circuits for **a** QND measurement tomography of generic measurements, **b** single-qubit gate set tomography, and **c** single-qubit and **d** two-qubit QND measurement tomography. **e**, **f** Schemes of IBM quantum devices (**e**) *ibm_perth* (7 qubits) and (**f**) *ibm_brooklyn* (65 qubits). Measurements of pairs of qubits connected by a bar of the same color (red, green and yellow) are characterized simultaneously in one run of the parallel tomography.

operators $\{\Upsilon_n\}$ whose matrix elements are given by[47]

$$\Upsilon_n^{ijkl} = \langle ij|\Upsilon_n|kl\rangle = \langle i|\mathcal{E}_n(|k\rangle\langle l|)|j\rangle, \qquad (1)$$

with $\{|i\rangle\}$ the basis of the measured system with dimension d. In terms of these matrices, we can conveniently determine the dynamics of the post-measurement states $\mathcal{E}_n(\rho) = \sum_{ijkl}\Upsilon_n^{ijkl}\rho^{kl}|i\rangle\langle j|$, the POVM elements $\Pi_n = \sum_{ijk}\Upsilon_n^{kjki}|i\rangle\langle j|$, and the measurement statistics $p(n) = \mathrm{Tr}\{\Pi_n\rho\}$, where $\rho^{kl} = \langle k|\rho|l\rangle$ are the components of the density matrix before measurement. Note that Υ_n is the transposed of the positive Choi operator $\tilde{\Upsilon}_n$, whose components are related by $\langle ij|\Upsilon_n|kl\rangle = \langle ik|\tilde{\Upsilon}_n|jl\rangle$[54].

The Choi matrices Υ_n^{ijkl} are a complete description of the quantum processes of a system and from them, we can extract all the relevant physical properties of the measurements. We discuss three relevant quantifiers of the measurement: the readout fidelity F, the QNDness Q, and the destructiveness D[47] (see methods). Comparing them, we can quantify the quality of the measurement for particular tasks and discriminate between different types of measurements. The readout fidelity F describes the efficiency of the readout irrespective of the post-measurement state, and it is thus maximal when the POVMs are projectors, $\Pi_n = |n\rangle\langle n|$. Operationally, it is defined as the average probability of successfully detecting a state $|n\rangle$ of the computational basis, after preparing the system in the same state. The QNDness Q is the fidelity with respect to an ideal measurement of an observable O, that is, a measurement that projects the states into the eigenvectors $|n\rangle$ of O and whose Choi matrices are projectors, $\Upsilon_n = |nn\rangle\langle nn|$. QNDness incorporates information on the post-measurement states and can be determined by the average probability that states of the computational basis $|n\rangle$ are preserved in two consecutive measurements. Finally, the destructiveness D quantifies the back-action introduced by the measurement[47]. For $D = 0$, the measurement is exactly QND which means that it preserves the expected value of the observable O after consecutive measurement $\langle O\rangle = \mathrm{Tr}[O\rho] = \mathrm{Tr}[O\mathcal{E}(\rho)]$. For $D > 0$, the destructiveness signals a deviation from the QND condition, which can occur independent of how ideal the measurement is. Therefore, it is convenient to know the three quantifiers F, Q, and D to provide a more complete analysis of general non-destructive measurements.

Our QND-MT protocol[47] reconstructs the Choi matrices of a QND measurement self-consistently. As shown in Fig. 1a, it consists of two applications of the measurement interspersed by a unitary gate V_i that prepares a complete basis of initial states, and a second gate U_j that enables a complete set of measurements. Given sufficient statistics, this protocol provides conditional probability distributions of single QND measurements $p(n|i)$ and
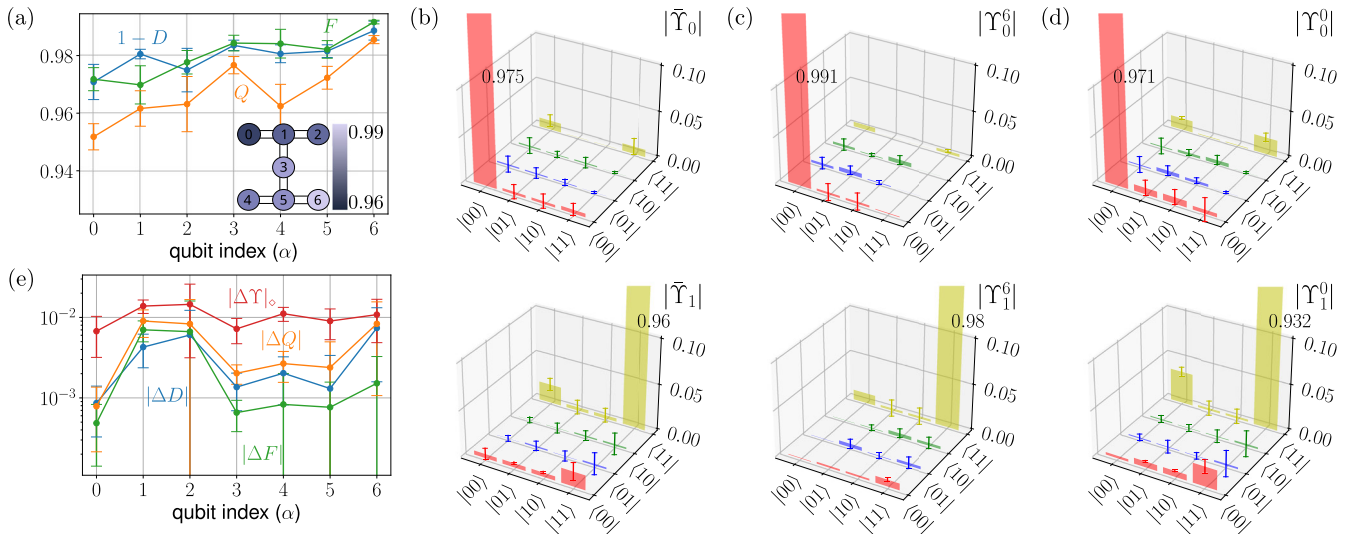
of consecutive measurements $p(nm|ij)$. A maximum-likelihood-based classical post-processing[55–57] transforms $p(n|i)$ and $p(nm|ij)$ into a set of physically admissible set of POVM elements $\{\Pi_n\}$ and Choi matrices $\{\Upsilon_n\}$, requiring to solve a total of $\mathcal{N} + 1$ optimization problems, with $\mathcal{N}$ the number of outcomes (see methods). The full characterization of QND detectors with N qubits and $\mathcal{N} = 2^N$ possible outcomes demands reconstructing 2^N Choi operators of size 4^N. In the general case, using a strategy based on Pauli observables, QND-MT requires a total of 18^N circuits, corresponding to 6^N initial gates prepared with the tensor product of $V_i \in \{I, \sigma_x, e^{\mp i\pi\sigma_y/4}, e^{\mp i\pi\sigma_x/4}\}$ and 3^N intermediate unitaries given by the tensor products of $U_i \in \{I, e^{-i\pi\sigma_y/4}, e^{-i\pi\sigma_x/4}\}$, with I and σ_j the identity and Pauli operators. Figure 1b–d shows the circuits for the particular case of a single qubit and two qubits, as explained below.

The exponential scaling in the number of circuits makes QT—in the QND-MT or in any other form—unfeasible for systems with large numbers of qubits. This scaling may be avoided if the measurements of separate quantum subsystems are shown to be independent. QND measurements in superconducting circuits are implemented via dispersive readout[15–17], where each qubit is coupled to an off-resonance cavity, on which one performs homodyne detection to individually extract the outcome of each qubit state. These readouts are thus built to be independent of each other, but imperfections in the device can lead to crosstalk between the qubit measurements[26,58]. Nevertheless, these correlations can be characterized by two-qubit QND-MT of each pair of qubits. If the correlations are weak enough, it is possible to execute a highly parallelized and scalable QND-MT for multi-qubit detectors, reducing the number of circuits and the classical post-processing time.

Parallel single-qubit QND measurement tomography

Let us first discuss the tomographic reconstruction of every single-qubit measurement of a quantum processor with N qubits. This means using QND-MT to reconstruct $2N$ single-qubit Choi matrices Υ_n^α, for qubits $\alpha = 1, ..., N$ and $n = 0, 1$. Single-qubit QND-MT applies two measurements Υ_n^α in between single-qubit gates V_i and U_j, as shown in Fig. 1c, requiring the evaluation of 18 different circuits. For each pair of measurement outcomes, the associated Choi matrix Υ_n^α is estimated as the solution of a maximum likelihood optimization problem.

Initialization and gate errors are accounted for in this optimization by means of single-qubit GST[48,59–61]. GST self-consistently characterizes the initial state, the final POVM measurement, and a complete set of linearly independent gates G_i of a device. In our case, $G_i \in \{I, \sigma_x, e^{-i\pi\sigma_y/4}, e^{-i\pi\sigma_x/4}\}$ are the gates used to implement all the V_i and U_i operations from QND-

Fig. 2 Experimental tomographic characterization of single-qubit measurements in parallel. a Measurement quantifiers: fidelity F (green), QNDness Q (orange), and indestructiveness $1 - D$ (blue) for each qubit. The inset represents the average performance $(F + Q + 1 - D)/3$ of each qubit, as they are located on the *ibm_perth* quantum processor. **b** Average Choi matrices $\overline{\Upsilon}_n$ of all qubits for both measurement outcomes $n = 0, 1$. **c, d** Specific Choi matrices Υ_n^6 and Υ_n^0 corresponding to the qubits with best and worst readout performance, respectively. **e** Error in the quantifiers and the Choi operators introduced by the parallelization of the QND-MT. Error bars are the standard deviation estimated with 5 realizations of the experiment.

MT. Note that GST requires 64 circuits, each composed of three gates G_i and a measurement, as shown in Fig. 1b.

The execution of the circuits of the N single-qubit QND-MTs and GST circuits can be efficiently parallelized, applying the single-qubit operations simultaneously as sketched in Fig. 1b, c. This reduces the total number of experiments from $\mathcal{O}(N)$ down to the sum of 18 QMD-MT and 64 GST circuits. With this refinement, we studied the readout of all qubits in the IBM quantum device *ibm_perth*. This processor has a quantum volume[62] of 32 and CLOPS (Circuit Layer operations per second) of 2.9×10^3 [63], and a qubit connectivity graph shown in Fig. 1e. Each circuit was evaluated with 2^{13} shots, resulting in an experiment that takes approximately 2 min, with classical post-processing of 30 s on a Ryzen-7 5800H processor with eight cores.

From the reconstructed Choi matrices of each qubit, we derived the three quantifiers—readout fidelity F, the QNDness Q, and the indestructiveness $1 - D$—shown in Fig. 2a. The *ibm_perth* processor exhibits readout fidelities between 0.969 and 0.992, with an average of $\overline{F} = 0.98$. QNDness varies much more along the device, ranging from 0.951 in the qubit $a = 0$–0.987 in $a = 6$, with an average of $\overline{Q} = 0.967$. Indestructiveness behaves similarly to fidelity except for qubit $a = 1$ and ranges between 0.97 and 0.991. The arithmetic mean of F, Q, and $1 - D$—see colormap in Fig. 2a—characterizes the performance across the device: qubits in the upper sector ($a = 0, 1, 2$) perform notably worse than those in the lower half of the chip.

The Choi matrices not only provide individual qubit metrics (F, Q, D) but also hint at the physical processes behind measurement errors. The Choi matrix element $p_n^{a \to b} = \langle bb | \Upsilon_n | aa \rangle$ quantifies the probability that the state flips from $|a\rangle$ to $|b\rangle$ when outcome n is detected. Each element informs about deviations from the ideal projective measurement $p_a^{a \to a} = 1$, as well as possible origins for those deviations.

Let us first put this into practice using the averaged Choi matrices $\overline{\Upsilon}_n = \sum_a \Upsilon_n^a / N$, shown in Fig. 2b. Note how the readout of the $|0\rangle$ state ($p_0^{0 \to 0} = 0.975$) is implemented with better quality than that of $|1\rangle$ ($p_1^{1 \to 1} = 0.960$). Bit-flip noise is identified as the main source of errors, dominated by the qubit decay process $|1\rangle \to |0\rangle$ ($p_1^{1 \to 0} = 0.02$), and slightly less influenced by the excitation channel $|0\rangle \to |1\rangle$ ($p_1^{0 \to 1} = 0.016$). Considering that

ibm_perth has a relaxation time $T_1 \approx 100 \, \mu s$ and a measurement time $T = 700 \, ns$ [19], we estimate a baseline probability of qubit relaxation $p_{th} = 1 - e^{-T/T_1} \approx 0.007$, which accounts for 35% of the observed decay error. The remaining bit-flip error may be due to Purcell-induced decay and other non-dispersive errors that occur during the measurement process itself[47].
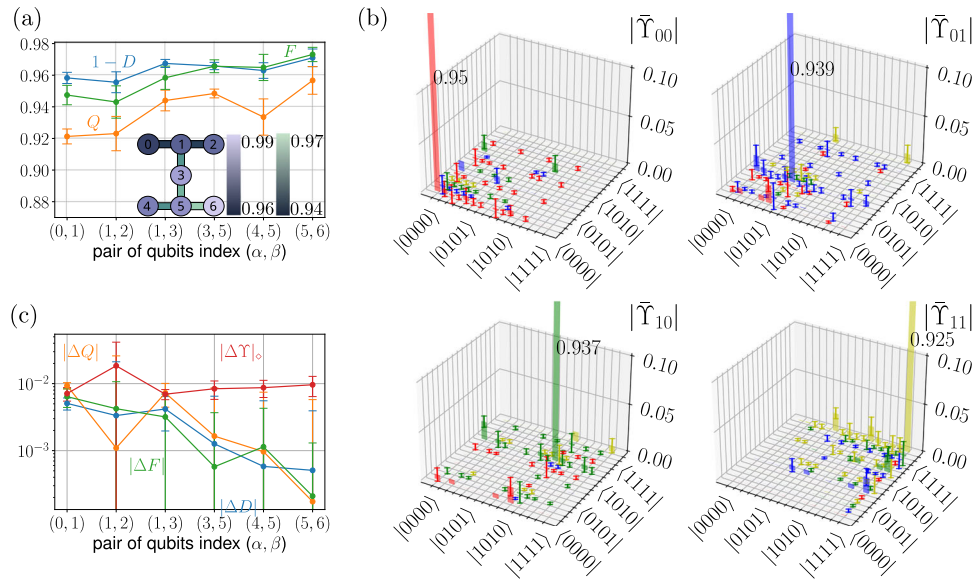
This analysis may also be done qubit by qubit. Figure 2c, d shows the experimental Choi matrices for qubits $a = 6$ and $a = 0$, respectively (all others being included in Supplementary Fig. 1). Qubit $a = 6$ is the best on the device, with $F = 0.991$, $Q = 0.985$, and $1 - D = 0.988$. Its Choi matrices are also the closest ones to an ideal measurement, with large values of $p_n^{n \to n}$ and below average flip errors. On the other hand, Qubit $a = 0$ is the one exhibiting the worst performance with $F = 0.971$, $Q = 0.951$, and $1 - D = 0.97$. The Choi matrices for this qubit are dominated by a strong bit-flip error $p_1^{1 \to 0} = 0.035$ and $p_1^{0 \to 1} = 0.021$ in the outcome $|1\rangle$, and non-dispersive errors given by elements $\langle ab | \Upsilon_0 | 00 \rangle$ and $\langle ab | \Upsilon_1 | 11 \rangle$, with $a \neq b$. The projection in this outcome is thus not done correctly, which explains the reduction in the QNDness and indestructiveness.

The parallelized tomography of the qubits has obvious performance advantages, but it could increase the error of the operations[25]. To quantify potential deviations, we have compared the outcome of parallel tomography on *ibm_perth* with the independent characterization of those qubits, running the $\mathcal{O}(N)$ circuits separately. As shown in Fig. 2e, the differences in the three quantifiers—fidelity $|\Delta F| = |F_{ind} - F_{par}|$, QNDness $|\Delta Q| = |Q_{ind} - Q_{par}|$, and destructiveness $|\Delta D| = |D_{ind} - D_{par}|$—lay below 10^{-2}, and are smaller than the non-idealities of those quantifiers (see Fig. 2a). Similarly, we have quantified the average distance in diamond norm[64,65] between the Choi operators computed using both strategies $|\Delta \Upsilon|_\diamond = |\Upsilon_{ind} - \Upsilon_{par}|_\diamond \leq 1$, and these lay below 1.4×10^{-2} (see Fig. 2e), validating the use of the parallelized strategy.

Two-qubit QND measurement tomography and crosstalk quantification

The low distinguishability between parallel and independent single-qubit QND-MT suggests that measurement correlations are weak across the device. We can further quantify such correlations

Fig. 3 Experimental tomographic characterization of two-qubit measurements over every pair of connected qubits in parallel. **a** Measurement quantifiers F, Q, and $1-D$ for each nearest-neighbor pair. The inset represents the average performance $(F+Q+1-D)/3$ in the device of each qubit (blue color code in circles) and of every pair of connected qubits (green color code in bars). **b** Reconstructed two-qubit Choi matrices $\overline{\Upsilon}_{nm}$ averaged over all connected pairs of qubits for the four possible outcomes with $n, m = 0, 1$. **c** Error in the quantifiers F, Q, and $1-D$ and the Choi operators introduced by the parallelization. Error bars are the standard deviation estimated with 5 realization of the experiment.

comparing the joint measurement process for pairs of qubits (a, β), given by $\Upsilon_{mn}^{\alpha\beta}$ for outcomes $m, n = 0, 1$, with the individual measurement processes $\Upsilon_m^\alpha \otimes \Upsilon_n^\beta$.

The two-qubit QND-MT requires the evaluation of 324 circuits—two measurement processes interspersed by layers of gates V_i and U_j (cf. Fig. 1d). Since characterizing all $N(N-1)/2$ pairs on an N-qubit device is very costly, we first focused on neighboring qubits, which we expect to exhibit the greatest correlations. More precisely, for a device with M physical connections $(a, \beta) \in \mathcal{C}$ of M, we aim to reconstruct the $4M$ two-qubit Choi matrices.

This two-qubit QND-MT can be parallelized by executing similar circuits on non-overlapping pairs of physically connected qubits. This requires dividing the quantum processor into sets of edges that do not share a common qubit. For the 7-qubit ibm_perth and the 65-qubit ibm_brooklyn quantum processors, illustrated in Fig. 1e, f, we only need three sets. For a generic planar graph with M vertices, coloring theorems[66] ensure that the number of sets is never larger than 4, setting a bound on the number of circuits 4×18^2 that does not grow with the processor's size. Finally, the protocol requires solving $5M$ optimization problems, a task that can be efficiently parallelized on classical computers. Here, we employ a parallel two-qubit QND-MT to characterize the readout of physically connected qubits on the IBM quantum device ibm_perth. The experiment runs approximately in 38 min—using 2^{13} shots per circuit—and the post-processing in 3 min.

Figure 3a shows the experimental results for the quantifiers F, Q, and $1-D$ describing the two-qubit measurement. We see an overall decrease in the readout performance of pairs qubits with respect to the single-qubit results in Fig. 2a, but still we identify the same qualitative behavior: F and Q increase from top to bottom of the device (see inset of Fig. 3a) and QNDness is the worst and most fluctuating quantifier. As discussed below, the two-qubit quantifiers of all connected pairs are very well approximated as products of the single-qubit ones—e.g., $F^{\alpha\beta} \approx F^\alpha F^\beta$ and $Q^{\alpha\beta} \approx Q^\alpha Q^\beta$. This explains the reduction in average two-qubit fidelity and QNDness between pairs to $\overline{F} = 0.958$ and $\overline{Q} = 0.937$. Indestructiveness $1-D$ is the most stable quantifier, ranging between 0.955 and 0.97, but reduces its average in a similar amount to $1-\overline{D} = 0.963$.

Figure 3b shows the two-qubit Choi matrices averaged over all pairs of connected qubits, $\overline{\Upsilon}_{nm} = \sum_{(a,\beta) \in \mathcal{C}} \Upsilon_{nm}^{\alpha\beta}/M$. The Choi matrices for all pairs are included in Supplementary Fig. 2. The largest probabilities of type $p_{ab}^{ab \to ab} = \langle ab|\overline{\Upsilon}_{ab}|ab\rangle$ show the same behavior as $p_a^{a \to a} = \langle a|\Upsilon_a|a\rangle$ for the singe-qubit case. The lowest deviation from the ideal measurement corresponds to the state $|00\rangle$ ($p_{00}^{00 \to 00} = 0.95 \approx (p_0^{0 \to 0})^2$), followed by $|01\rangle$ and $|10\rangle$ ($p_{01}^{01 \to 01} = p_{10}^{10 \to 10} = 0.938 \approx p_0^{0 \to 0}p_1^{1 \to 1}$), and finally the two-excitation state $|11\rangle$ (with $p_{11}^{11 \to 11} = 0.924 \approx (p_1^{1 \to 1})^2$), which suffers more from bit-flip errors.
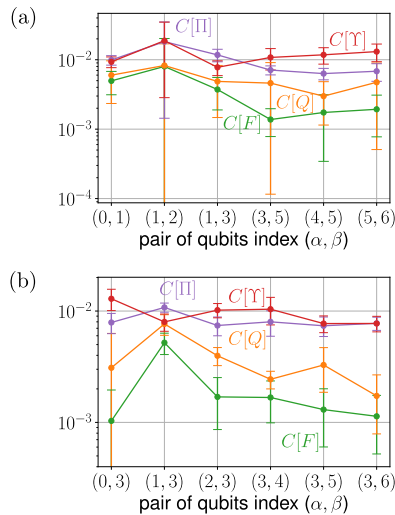
As in the single-qubit case, we estimate the errors introduced by parallelization by comparing the parallelized two-qubit QND-MT with the independent tomography of each pair. Figure 3c shows the error in fidelity, QNDness, destructiveness, and Choi operators for each pair of physically connected qubits, as defined in the previous section. Parallelization introduces an error below 2×10^{-2} in all quantifiers and Choi operators.

We quantify the measurement crosstalk by comparing the measurement processes of individuals and pairs of qubits. This is done at the level of quantifiers, introducing heuristic measures of separability for the fidelity $C[F^{\alpha\beta}] = |F^{\alpha\beta} - F^\alpha F^\beta|$ and for the QNDness $C[Q^{\alpha\beta}] = |Q^{\alpha\beta} - Q^\alpha Q^\beta|$. It is also done at the level of operators, with estimates of the POVM correlation $C[\Pi^{\alpha\beta}]$ and the Choi correlation $C[\Upsilon^{\alpha\beta}]$ (see Methods).

As hinted above, we observe a good separability of quantifiers. In Fig. 4a we see correlations of ibm_perth device below 10^{-2} for all pairs, allowing us to estimate the fidelity and QNDness of pairs of qubits as products of the properties of individual qubits.

Figure 4a shows the POVM and Choi correlations for the ibm_perth device. We certify the presence of measurement crosstalk between all physically connected pairs of qubits: all POVM elements and Choi matrices are non-separable with correlations on the order of 10^{-2}, which exceed the statistical error bars from the tomography for most of the qubits. This represents a crosstalk error of about 1%, which is smaller than the physical error found on single- and two-qubit tomography.

QND-MT is not restricted to nearest-neighbor correlations. As an example, we have analyzed the correlations between all qubits in ibm_perth and the central qubit $a = 3$, in 6 sets of separate

(a)

(b)

Fig. 4 Correlations in the joint measurement of pairs of qubits obtained by QND-MT. a Correlations in fidelity $C[F]$, QNDness $C[Q]$, and Choi operators $C[\Upsilon]$ for the joint readout of each pair of physically connected qubits. **b** Same correlations $C[F]$, $C[Q]$, and $C[\Upsilon]$ for the readout of qubit $a = 3$ with every other qubit of the device.

experiments. This produces pairs at two different distances, the first neighbors $(1, 3)$ and $(3, 5)$, and the second neighbors $(0, 3)$, $(2, 3)$, $(3, 4)$, and $(3, 6)$. Figure 4b shows the correlations obtained for those pairs. We can see that correlations $C[F^{\alpha\beta}]$ and $C[Q^{\alpha\beta}]$ are of order 10^{-3} for all qubits, while $C[\Pi^{\alpha\beta}]$ and $C[\Upsilon^{\alpha\beta}]$ are approximately 10^{-2}. In this small device, we do not observe a clear decay of correlations with distance, but we verify that all correlations are smaller than the measurement errors detected for independent single-qubit tomography.

Scaling of QND-MT on larger devices

Parallel single-qubit QND-MT is an efficient technique to characterize large devices that requires a fixed number of circuits—82 including GST—independently of the device size. Using the execution times obtained in the experiments on the *ibm_perth* we can extrapolate the performance in larger devices. For the 65-qubit *ibm_brooklyn*, with a degree 3 connectivity shown in Fig. 1f and a smaller CLOPS number of 1.5×10^{3} [63], we estimate 4 min for the single-qubit characterization and 5 min of post-processing in a Ryzen-7 5800H processor with 8 cores. Notice that all experimental execution times do not depend on the size of the device, but they are limited by the number of CLOPS, which are typically lower for larger devices.

We have discussed also three strategies to certify the errors in parallel QND-MT. One strategy is the application of QND-MT of individual qubits in separate, non-parallel experiments. This has a cost that grows linearly $\mathcal{O}(N)$ with the number of sampled qubits, but it is a routine that may be applied with less frequency than the complete calibration. This method enables the development of heat maps of the chip and suggests the order of magnitude of underlying correlations.

The second strategy is the parallelized QND-MT of pairs of neighboring qubits, a method that will provide results consistent with the previous methodology, but also give information about the strength of the crosstalk. In the two-qubit parallelized strategy, our estimate gives a total of 1296 independent circuits for any device size, taking 63 min for the two-qubit circuit evaluation in a 65-qubit *ibm_brooklyn* processor, and 30 min in a Ryzen-7 5800H processor with eight cores.

The third and most expensive strategy is to implement a two-qubit QND-MT for *all qubit pairs* in large devices with $O(\log(N))$

parallel groups[67] and $O(N^2)$ optimization problems. In this case, we estimate 2.5 h for the experiment and a similar amount of post-processing to characterize the *ibm_brooklyn* device. This is an efficient scaling that enables a very robust calibration of the complete device, to be done only sporadically.

Finally, for larger devices, the execution and post-processing times could be too long for a complete two-qubit MT—extending to days for devices with more than 1000 qubits—in which case it makes sense to either randomly sample those pairs, or concentrate the study to specific regions of the chip, that revealed more problematic in the first two methods.

QND measurement tomography of generalized measurements

The QND-MT protocol we introduce can be applied to any kind of generalized measurements[2]. These include synthetic measurements that combine standard detectors with other computing elements, such as local and entangling gates, auxiliary qubits, and resets.
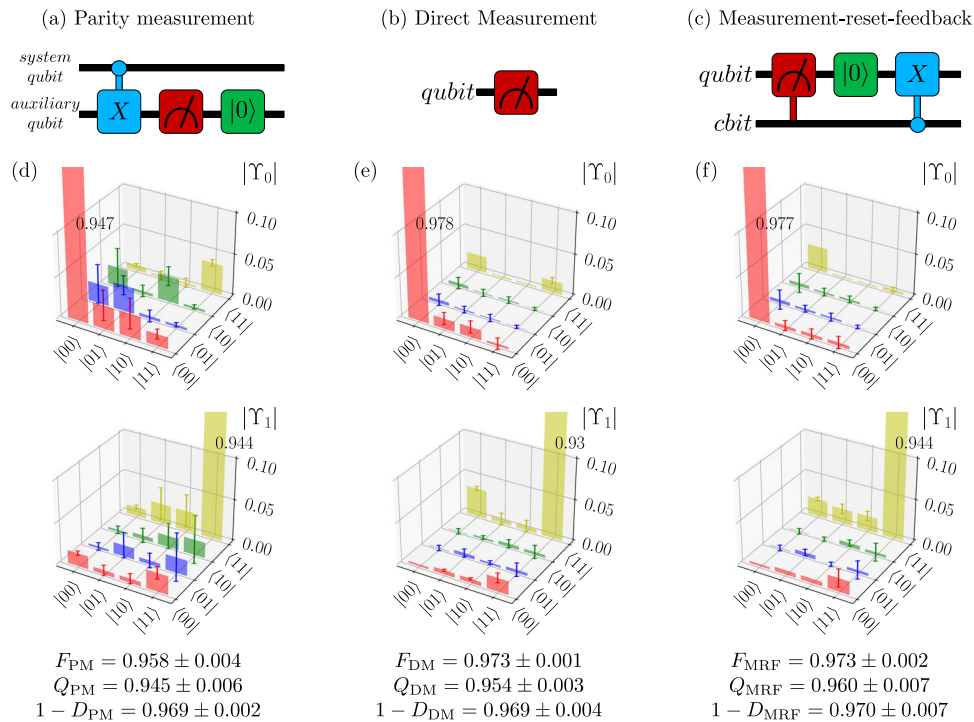
In this work, we discuss the application to stabilizer measurements, a relevant example which are widely used in quantum error correction protocols[18,29,30]. Such measurements are usually implemented with controlled operations over an auxiliary qubit, which is finally measured and reset, to discriminate states with different stabilizer values. If we trace over the auxiliary qubit, the generalized measurement is, up to implementation errors, QND, enabling the repetitive monitoring of error syndromes.

As an illustration of how QND-MT works with a generalized measurement, we discuss a single-qubit PM. As shown in Fig. 5a, this protocol includes an auxiliary qubit, a controlled CNOT operation, and a single-qubit readout and reset. Note that, unlike all higher PMs, the single-qubit PM does not entangle multiple system qubits and thus it is not directly applicable to quantum error correction codes. However, it already includes all the underlying operations supporting multi-qubit PM, which can be scaled to characterize multi-qubit measurement errors in practical error correction codes. Here, we study the performance of the single-qubit PM using two fixed qubits of the *ibm_perth* quantum processor, and we compare it with the performance of the direct measurement (DM) on the same system qubit, as shown in Fig. 5b. The Choi matrices and the quantifiers obtained for the parity and DMs are shown in Fig. 5d, e, respectively.

In this study, we observe a decrease in the fidelity and QNDness of the PM with respect to DM. The readout fidelity of the PM $F_{PM} = 0.958$ is close to the product of $F_{DM} = 0.973$ and the fidelity of the CNOT provided by IBM $F_{CNOT} = 0.9897$. Therefore, we can conclude that this decrease is mainly due to the CNOT gate as the error from reset is expected to be smaller than 1% [68]. The indestructiveness is the same for parity and DMs, $1 - D_{PM} = 1 - D_{DM} = 0.969$, which is consistent with the fact that the CNOT and reset operations do not add measurement back-action to the system. In the Choi operators, we can also see the appearance of new bars that describe the noise introduced by the CNOT gate, as well as an increase in the overall error bars and fluctuations.

Another interesting example of generalized measurement is the measure-reset-feedback (MRF) operation, shown in Fig. 5c. It consists of a QND measurement followed by a reset and a classically conditioned NOT operation that brings the measured qubit exactly to the quantum state selected as measurement outcome—i.e., the qubit is reset to state $|0\rangle$ or $|1\rangle$ when the measurement outcome was deemed $n = 0$ or 1, respectively. If the reset and NOT operations have high fidelities, measurement-and-reset should fix the QND nature of measurement, bringing the errors $1 - Q$ and D closer to the measurement infidelity $1 - F$.

We applied QND-MT to this generalized measurement using a single qubit of the IBM-Q *ibm_perth* processor. The resulting Choi matrices and quantifiers are shown in Fig. 5f. The MRF scheme has better performance than the DM in the same qubit, having

Fig. 5 Experimental QND-MT characterization of generalized measurements. Circuits depicting **a** a single-qubit parity measurement via an auxiliary qubit, **b** a direct qubit measurement, and **c** a measurement-and-reset scheme with classical feedback. **d**–**f** Choi matrices and quantifiers corresponding to each scheme. Error bars are the standard deviation estimated from 5 realization of the experiments.

approximately the same fidelity $F_{DM} \approx F_{MRF} \approx 0.975$ and indestructiveness $1 - D_{DM} \approx 1 - D_{MRF} \approx 0.969$, but with an increase of QNDness from $Q_{DM} = 0.954$ to $Q_{DM} = 0.960$. Considering the error bars of the QNDness and indestructiveness, we find that the worst-case MRF provides a QND readout with the same quality as a DM. Moreover, we also witness a reduction in the noisy components of the Choi operator, such as those describing bit-flip errors.

DISCUSSION

In this work, we have demonstrated an efficient, highly parallelizable protocol for QND-MT of a state-of-the-art multi-qubit quantum computer, which works with both single-qubit measurement and generalized measurement—e.g., error syndrome measurements, PMs, etc. Our method is based on a self-consistent reconstruction of the Choi matrices for single-qubit and two-qubit measurements, which provides information about measurement quality, the QND nature of the measurement and the strength and type of errors.

In the single-qubit scenario, we have developed strategies to massively parallelize the tomography, an approximation that works when multiple measurements can be executed with small crosstalk or correlation. We have applied this protocol in experiments with a 7-qubit IBM quantum computer, obtaining fascinating insight into the performance of the device. First of all, we have found that the chip is well tuned to high-fidelity measurements, with weak and long pulses—much longer than single- or two-qubit gates—that mitigate non-dispersive and discrimination errors, at the expense of increasing incoherent errors, in particular, single-qubit bit flip. This limits the QND nature of the measurement which fluctuates along the different qubits of the device.

We have also developed different strategies to determine whether single-qubit measurements are independent, and can be parallelized. The most sophisticated strategy involves applying QND-MT to the simultaneous measurement of two qubits, to reconstruct the joint Choi matrices and quantify the degree of correlation. In the setup considered, these correlations lay below 1% and validate the parallelization strategy which, as discussed above, can be efficiently scaled to large multi-qubit processors with an almost fixed cost.

Finally, we have also demonstrated how QND-MT can be generalized to custom measurements, in particular to parity-type measurements relevant to quantum error correcting codes and measurement-and-reset schemes with classical feedback. We used the Choi matrices to identify coherent errors introduced by the CNOT gate in PMs and we provided evidence that the reset operation with classical feedback is an appealing way to improve the QND quality of a measurement.

This work opens several avenues for further research. The obvious one is to use QND-MT as an input for the systematic optimization of the measurement pulses. The goal here is to optimize the driving amplitude and measurement time, minimizing the errors that manifest in the Choi matrices. This would allow us to reduce the decay channels found in the experiment, while keeping other sources of error at bay—e.g., non-dispersive effects[21], discrimination errors[47,69], decoherence[20], leakage to higher levels of the transmon[23], or rotating wave corrections[22]. Another approach is to design alternative schemes for qubit readout that may be more QND[49,50,70], but this would add new error sources that could be similarly identified and characterized with the application of QND-MT.

An additional research avenue is to further understand and mitigate the correlations between simultaneous measurements. In this work, we have explored two-qubit correlations, but higher-order correlations, involving three or more qubits, could also be analyzed with the help of better tomography methods, such as compressed sensing[71,72]. These methods could also be used to quantify readout and crosstalk errors occurring in multi-qubit stabilizer measurements involving plaquettes of four or more qubits as they are required in practical quantum error correction codes such as the surface[18,29,30] or color codes[73].

METHODS

QND measurement quantifiers

To characterize the most important properties of non-destructive measurements, we employ three quantifiers: the readout fidelity, the QNDness, and the destructiveness. Here, we show how to obtain these quantifiers from the reconstructed Choi matrices as introduced in ref. [47].

The fidelity F is the standard quantifier of a detector's readout performance, measured by the probability that an initially prepared eigenstate $|n\rangle$ is successfully identified,

$$F = \frac{1}{2^N} \sum_{n=0}^{2^N-1} \langle n|\Pi_n|n\rangle. \tag{2}$$

The fidelity can be interpreted as the efficiency of the readout as it can be related to the signal-to-noise ratio of the measurement[15,70]. It ignores any information about the post-measurement state and the QND nature of the measurement. The QNDness Q incorporates information from the post-measurement state and quantifies how close are the Choi matrices with respect to an ideal projective measurement. In quantitative terms, it is the probability that an initially prepared eigenstate $|n\rangle$ is preserved and successfully identified in two consecutive measurements,

$$Q = \frac{1}{2^N} \sum_{n=0}^{2^N-1} \langle nn|\Upsilon_n|nn\rangle. \tag{3}$$

The destructiveness D[47] asserts precisely the QND nature of generic measurements by verifying the preservation of the expectation value $\langle O \rangle$ after the measurement. Operationally, it is defined as the largest change suffered by any observable compatible with O as:

$$D = \frac{1}{2} \max_{\|O_c\|=1} \|O_c - \mathcal{E}^\dagger(O_c)\|, \quad [O, O_c] = 0, \tag{4}$$

where $\|\cdot\|$ is the Hilbert–Schmidt norm. Unlike F and Q, computing D requires a complete tomographic reconstruction of the measurement process, $\mathcal{E}^\dagger(O_c) = \sum_{ijkln} \left[\Upsilon_n^{klij}\right]^* O_c^{kl} |i\rangle\langle j|$, but it allows us to quantify the measurement back-action without the bias of Q toward ideal measurements[47]. Note that Eq. (4) is motivated by the definition of a QND measurement, $\mathrm{Tr}(O\rho) = \mathrm{Tr}(O\mathcal{E}(\rho))$. Moving into the Heisenberg picture this condition becomes $\mathrm{Tr}(O\rho) = \mathrm{Tr}(\mathcal{E}^\dagger(O)\rho)$, where $\mathcal{E}^\dagger$ is the self-adjoint process of $\mathcal{E}$. Therefore, we can quantify how QND is a measurement by the deviation between O and $\mathcal{E}^\dagger(O)$, that is $\|O - \mathcal{E}^\dagger(O)\|$. The last step to obtain Eq. (4) consists in searching for the largest disagreement over the set of all normalized observables compatible with O, so that we ensure that D is an upper bound for the back-action of the measurement.

Quantification of measurement crosstalk and correlations

To quantify the correlations in the measurement of pairs of qubits, we introduce heuristic metrics that compare the POVM and Choi matrices derived from two-qubit tomography with the tensor product of the operators obtained from single-qubit tomography. Although this is a comparison between two detector models rather than an intrinsic property of the operators, the outcome provides information about the operation of the device and the effect of including higher-order interactions in the QND-MT. We also use these correlations to quantify the distinguishability error of performing the tomography in parallel or independently, as shown below.

First, we define the correlation in two-qubit Choi operators $C[\Upsilon^{\alpha\beta}]$. Let Υ_n^α and Υ_m^β be the process operators of two single qubits α and β, and let $\Upsilon_{nm}^{\alpha\beta}$ be the joint measurement of both

qubits. We define the Choi matrices correlation as:

$$C[\Upsilon^{\alpha\beta}] = \frac{1}{8} \sum_{nm} ||\Upsilon_{nm}^{\alpha\beta} - \Upsilon_n^\alpha \overline{\otimes} \Upsilon_m^\beta|| \tag{5}$$

where $\overline{\otimes}$ is tensor product operation in the super-operator space and $\|\cdot\|_\diamond$ is the diamond norm[64,65]. This quantity not only evaluates the distance between the processes $\Upsilon_n^\alpha \overline{\otimes} \Upsilon_m^\beta$ and $\Upsilon_{nm}^{\alpha\beta}$, but is also related to the probability of discriminating the quantum states generated by them. This probability is given by $P_d = (1 + C[\Upsilon^{\alpha\beta}])/2$. Therefore, a small $C[\Upsilon^{\alpha\beta}] \ll 1$ means that the post-measurement states are nearly indistinguishable. Notice that the pre-factor in $C[\Upsilon^{\alpha\beta}]$ is chosen to normalize the correlation between 0 and 1.

Conveniently, we can use the same definition in Eq. (5) to evaluate the distinguishability of Choi matrices reconstructed in parallel Υ_{par} or independently Υ_{ind} as $C[\Delta\Upsilon] = C[\Upsilon_{par} - \Upsilon_{ind}]$, and thereby quantify the error introduced by the parallelization. This is done in Figs. 2e and 3c.

In a similar spirit as done for $C[\Upsilon^{\alpha\beta}]$, we can define the correlation $C[\Pi^{\alpha\beta}]$ in the POVMs of two-qubit measurements. Let Π_n^α and Π_m^β be the POVM elements of two single qubits α and β, and $\Pi_{nm}^{\alpha\beta}$ be the joint POVM element of both qubits. We define the POVM correlation as:

$$C[\Pi^{\alpha\beta}] = \frac{1}{4} \sum_{nm} ||\Pi_{nm}^{\alpha\beta} - \Pi_n^\alpha \otimes \Pi_m^\beta||_2, \tag{6}$$

where $\|\cdot\|_2$ is the 2-norm, that is, the largest singular value. This quantity establishes an upper bound for the average error on the probability distribution predicted by the single-qubit reconstruction $P_{nm}^S = Tr(\rho[\Pi_n^\alpha \otimes \Pi_m^\beta])$ compared with the joint measurement $P_{nm}^J = Tr(\rho\Pi_{nm}^{\alpha\beta})$, given by $\sum_{nm} |P_{nm}^S - P_{nm}^J|/4 \leq C[\Pi^{\alpha\beta}]$ for any density matrix ρ. Notice that $C[\Pi^{\alpha\beta}]$ is normalized between 0 and 1 as $C[\Upsilon^{\alpha\beta}]$.

Maximum likelihood estimation for QND measurement tomography

Maximum likelihood estimation (MLE) is a statistical inference method widely used in QT. MLE allows us to recover density matrices, POVMs, or Choi matrices that are meaningful and satisfy all the physical constraints of a measurement. It achieves this goal by optimizing the likelihood function $\mathcal{L}(\theta|\hat{f})$ of the experimental data $\hat{f}$ for a given parametric model $\mathcal{M}(\theta)$. We employ a Gaussian distribution as a likelihood function,

$$\mathcal{L}(\theta|\hat{f}) = \sum_i \frac{[\hat{f}(i) - p(i)]^2}{p(i)}, \tag{7}$$

where $\hat{f}(i)$ are the estimated probabilities obtained from the experiment and $p(i)$ are the theoretical probabilities predicted by the model $\mathcal{M}(\theta)$. We minimize this likelihood function (7) for both the QND-MT and GST. Notice that, for simplicity, the notation of the theoretical probabilities $p(i)$ omits the dependence on the parameters θ, and that the index i may refer to a group of indices as shown below.

The QND-MT consists of two steps, first an MT of the POVM and then a process tomography of each Choi matrix. We reconstruct the POVMs $\{\Pi_j\}$ by first obtaining the theoretical probabilities,

$$p(n|k) = \mathrm{Tr}(\Pi_n V_k(\rho)), \tag{8}$$

of obtaining the outcome n condition to the application of gate V_k. We then minimize the likelihood function of form (7) over the set of feasible matrices $\{\Pi_n\}$ satisfying $\Pi_n \geq 0$ and $\sum_n \Pi_n = \mathbb{1}$. Finally, we estimate the Choi matrices Υ_n by obtaining the theoretical probabilities,

$$p(mn|jk) = \mathrm{Tr}[(U_j^\dagger(\Pi_m) \otimes V_k(\rho)^T)\tilde{\Upsilon}_n], \tag{9}$$

of obtaining the outcome n in the second measurement and the outcome m in the first measurement, condition to the application

of gates j and k. We then minimize the corresponding likelihood function of the form (7) over the set of the Choi matrix Υ_n that satisfies $\tilde{\Upsilon}_n \geq 0$ and the POVM constraint $\mathrm{Tr}_1(\tilde{\Upsilon}_n) = \Pi_{\underline{n}}$. Here, $\mathrm{Tr}_1(\cdot)$ is the partial trace over the first subsystem, and $\tilde{\Upsilon}$ is the transposed Choi matrix, which is a positive matrix with elements $\langle ik|\tilde{\Upsilon}|jl\rangle = \langle ij|\Upsilon|kl\rangle$.

To separate experimental errors in gates and state preparation from the measurement errors that we want to characterize, we can apply a GST previously to the QND-MT. The GST gives us an experimental estimate of the set $\{\rho, \Pi_i, G_j\}$, composed of estimators of the initial state, the POVM elements, and the gates, respectively. Here $\{\mathcal{G}_j\}$ are generic trace-preserving processes and not necessarily unitary operations. The theoretical probabilities of obtaining the outcome l are

$$p(l|ijk) = \mathrm{Tr}(\Pi_l G_k G_j G_i(\rho)), \tag{10}$$

which are conditions for the application of gates i, j, k as shown by the circuits in Fig. 1b. We then minimize (7) by comparing the probabilities (10) with the experimental data to obtain a physically meaningful set $\{\rho, \Pi_i, G_j\}$ that self-consistently accounts for state preparation, gates, and measurement errors. Notice that when we use GST, we can omit the first step of QND-MT as we already have an experimental estimate of the POVMs $\{\Pi_i\}$. In addition, the gates $\{U_j\}$ and $\{V_k\}$ needed for the second step of QND-MT must be formed as concatenations of the $\{G_k\}$ processes in order to account for gate errors.

In total, QND-MT of the device requires solving $3N + 5M$ optimization problems. We solve them using sequential least-squares programming, satisfying the positivity of operators via Cholesky decomposition, and the completeness constraints via Lagrange multipliers.

To quantify the goodness-of-fit of our estimators, we employ the χ^2 test[74,75]. This is a standard tool for statistical hypothesis testing, that is, for rigorously deciding if there is enough evidence to reject a model. In our work, we apply this test to all single- and two-qubit Choi matrix reconstructions and demonstrate that the fits and models are in agreement with the experimental data within a standard confidence interval of 95%. See Supplementary Methods 1 for a detailed analysis and a description of the method.

DATA AVAILABILITY
The code and the data used to perform the tomographic reconstructions and generate the figures are publicly available in GitHub and Zenodo[76].

REFERENCES
1. Braginsky, V. B. & Khalili, F. Y. *Quantum Measurement* (Cambridge University Press, 1992).
2. Breuer, H.-P. & Petruccione, F. *The Theory of Open Quantum Systems* (Oxford University Press, 2002).
3. Leibfried, D., Blatt, R., Monroe, C. & Wineland, D. Quantum dynamics of single trapped ions. *Rev. Mod. Phys.* **75**, 281 (2003).
4. Raha, M. et al. Optical quantum nondemolition measurement of a single rare earth ion qubit. *Nat. Commun.* **11**, 1605 (2020).
5. Grangier, P., Levenson, J. A. & Poizat, J.-P. Quantum non-demolition measurements in optics. *Nature* **396**, 537 (1998).
6. Gleyzes, S. et al. Quantum jumps of light recording the birth and death of a photon in a cavity. *Nature* **446**, 297 (2007).
7. Distante, E. et al. Detecting an itinerant optical photon twice without destroying it. *Phys. Rev. Lett.* **126**, 253603 (2021).
8. Sathyamoorthy, S. R. et al. Quantum nondemolition detection of a propagating microwave photon. *Phys. Rev. Lett.* **112**, 093601 (2014).
9. Neumann, P. et al. Single-shot readout of a single nuclear spin. *Science* **329**, 542 (2010).
10. Robledo, L. et al. High-fidelity projective read-out of a solid-state spin quantum register. *Nature* **477**, 574 (2011).
11. Nakajima, T. et al. Quantum non-demolition measurement of an electron spin qubit. *Nat. Nanotechnol.* **14**, 555 (2019).
12. Xue, X. et al. Repetitive quantum nondemolition measurement and soft decoding of a silicon spin qubit. *Phys. Rev. X* **10**, 021006 (2020).
13. Wallraff, A. et al. Approaching unit visibility for control of a superconducting qubit with dispersive readout. *Phys. Rev. Lett.* **95**, 060501 (2005).
14. Gómez-León, A., Luis, F. & Zueco, D. Dispersive readout of molecular spin qudits. *Phys. Rev. Applied* **17**, 064030 (2022).
15. Blais, A., Grimsmo, A. L., Girvin, S. M. & Wallraff, A. Circuit quantum electrodynamics. *Rev. Mod. Phys.* **93**, 025005 (2021).
16. Vijay, R., Slichter, D. H. & Siddiqi, I. Observation of quantum jumps in a superconducting artificial atom. *Phys. Rev. Lett.* **106**, 110502 (2011).
17. Walter, T. et al. Rapid high-fidelity single-shot dispersive readout of superconducting qubits. *Phys. Rev. Applied* **7**, 054020 (2017).
18. Google Quantum AI. Exponential suppression of bit or phase errors with cyclic error correction. *Nature* **595**, 383 (2021).
19. IBM Quantum; https://quantum-computing.ibm.com/ (2021).
20. Boissonneault, M., Gambetta, J. M. & Blais, A. Dispersive regime of circuit QED: photon-dependent qubit dephasing and relaxation rates. *Phys. Rev. A* **79**, 013819 (2009).
21. Govia, L. C. G. & Wilhelm, F. K. Entanglement generated by the dispersive interaction: the dressed coherent state. *Phys. Rev. A* **93**, 012316 (2016).
22. Sank, D. et al. Measurement-induced state transitions in a superconducting qubit: beyond the rotating wave approximation. *Phys. Rev. Lett.* **117**, 190503 (2016).
23. Wang, C., Chen, M.-C., Lu, C.-Y. & Pan, J.-W. Optimal readout of superconducting qubits exploiting high-level states. *Fundam. Res.* **1**, 16 (2021).
24. Slichter, D. H. et al. Measurement-induced qubit state mixing in circuit QED from up-converted dephasing noise. *Phys. Rev. Lett.* **109**, 153601 (2012).
25. Rudinger, K. et al. Experimental characterization of crosstalk errors with simultaneous gate set tomography. *PRX Quantum* **2**, 040338 (2021).
26. Seo, S. & Bae, J. Measurement crosstalk errors in cloud-based quantum computing. *IEEE Internet Comput.* **26**, 26 (2022).
27. Cerezo, M. et al. Variational quantum algorithms. *Nat. Rev. Phys.* **3**, 625 (2021).
28. Bharti, K. et al. Noisy intermediate-scale quantum algorithms. *Rev. Mod. Phys.* **94**, 015004 (2022).
29. Krinner, S. et al. Realizing repeated quantum error correction in a distance-three surface code. *Nature* **605**, 669 (2022).
30. Zhao, Y. et al. Realization of an error-correcting surface code with superconducting qubits. *Phys. Rev. Lett.* **129**, 030501 (2022).
31. Calderbank, A. R. & Shor, P. W. Good quantum error-correcting codes exist. *Phys. Rev. A* **54**, 1098 (1996).
32. Steane, A. M. Error correcting codes in quantum theory. *Phys. Rev. Lett.* **77**, 793 (1996).
33. Fowler, A. G., Mariantoni, M., Martinis, J. M. & Cleland, A. N. Surface codes: towards practical large-scale quantum computation. *Phys. Rev. A* **86**, 032324 (2012).
34. Campbell, E. T., Terhal, B. M. & Vuillot, C. Roads towards fault-tolerant universal quantum computation. *Nature* **549**, 172 (2017).
35. Chamberland, C. et al. Building a fault-tolerant quantum computer using concatenated cat codes. *PRX Quantum* **3**, 010329 (2022).
36. Eisert, J. et al. Quantum certification and benchmarking. *Nat. Rev. Phys.* **2**, 382 (2020).
37. Banaszek, K., Cramer, M. & Gross, D. Focus on quantum tomography. *New J. Phys.* **15**, 125020 (2013).
38. Steffen, M. et al. Measurement of the entanglement of two superconducting qubits via state tomography. *Science* **313**, 1423 (2006).
39. Pereira, L., Zambrano, L. & Delgado, A. Scalable estimation of pure multi-qubit states. *npj Quantum Inf.* **8**, 57 (2022).
40. Gaikwad, A., Shende, K., Arvind & Dorai, K. Implementing efficient selective quantum process tomography of superconducting quantum gates on IBM quantum experience. *Sci. Rep.* **12**, 3688 (2022).
41. Häffner, H. et al. Scalable multiparticle entanglement of trapped ions. *Nature* **438**, 643 (2005).
42. Monz, T. et al. Realization of the quantum toffoli gate with trapped ions. *Phys. Rev. Lett.* **102**, 040501 (2009).
43. Klimov, A. B., Muñoz, C., Fernández, A. & Saavedra, C. Optimal quantum-state reconstruction for cold trapped ions. *Phys. Rev. A* **77**, 060303 (2008).
44. Agnew, M., Leach, J., McLaren, M., Roux, F. S. & Boyd, R. W. Tomography of the quantum state of photons entangled in high dimensions. *Phys. Rev. A* **84**, 062101 (2011).
45. Chapman, R. J., Ferrie, C. & Peruzzo, A. Experimental demonstration of self-guided quantum tomography. *Phys. Rev. Lett.* **117**, 040402 (2016).
46. Zambrano, L. et al. Estimation of pure states using three measurement bases. *Phys. Rev. Applied* **14**, 064004 (2020).

47. Pereira, L., García-Ripoll, J. J. & Ramos, T. Complete physical characterization of quantum nondemolition measurements via tomography. *Phys. Rev. Lett.* **129**, 010402 (2022).

48. Rudinger, K. et al. Characterizing midcircuit measurements on a superconducting qubit using gate set tomography. *Phys. Rev. Applied* **17**, 014014 (2022).

49. Touzard, S. et al. Gated conditional displacement readout of superconducting qubits. *Phys. Rev. Lett.* **122**, 080502 (2019).

50. Dassonneville, R. et al. Fast high-fidelity quantum nondemolition qubit readout via a nonperturbative Cross-Kerr coupling. *Phys. Rev. X* **10**, 011045 (2020).

51. Lundeen, J. S. et al. Tomography of quantum detectors. *Nature Phys.* **5**, 27 (2008).

52. Fiurášek, J. Maximum-likelihood estimation of quantum measurement. *Phys. Rev. A* **64**, 024102 (2001).

53. Chen, Y., Farahzad, M., Yoo, S. & Wei, T.-C. Detector tomography on IBM quantum computers and mitigation of an imperfect measurement. *Phys. Rev. A* **100**, 052315 (2019).

54. Milz, S., Pollock, F. A. & Modi, K. An introduction to operational quantum dynamics. *Open Syst. Inf. Dyn.* **24**, 1740016 (2017).

55. Fiurášek, J. Maximum-likelihood estimation of quantum measurement. *Phys. Rev. A* **64**, 024102 (2001).

56. James, D. F. V., Kwiat, P. G., Munro, W. J. & White, A. G. Measurement of qubits. *Phys. Rev. A* **64**, 052312 (2001).

57. Shang, J., Zhang, Z. & Ng, H. K. Superfast maximum-likelihood reconstruction for quantum tomography. *Phys. Rev. A* **95**, 062336 (2017).

58. Arute, F. et al. Quantum supremacy using a programmable superconducting processor. *Nature* **574**, 505 (2019).

59. Dehollain, J. P. et al. Optimization of a solid-state electron spin qubit using gate set tomography. *New J. Phys.* **18**, 103018 (2016).

60. Nielsen, E. et al. Gate set tomography. *Quantum* **5**, 557 (2021).

61. Rudinger, K. et al. Experimental characterization of crosstalk errors with simultaneous gate set tomography. *PRX Quantum* **2**, 040338 (2021).

62. Cross, A. W., Bishop, L. S., Sheldon, S., Nation, P. D. & Gambetta, J. M. Validating quantum computers using randomized model circuits. *Phys. Rev. A* **100**, 032328 (2019).

63. Wack, A. et al. Quality, speed, and scale: three key attributes to measure the performance of near-term quantum computers. Preprint at https://doi.org/10.48550/arXiv.2110.14108 (2021).

64. Benenti, G. & Strini, G. Computing the distance between quantum channels: usefulness of the Fano representation. *J. Phys. B: At. Mol. Opt. Phys.* **43**, 215508 (2010).

65. Blume-Kohout, R. et al. Demonstration of qubit operations below a rigorous fault tolerance threshold with gate set tomography. *Nat. Commun.* **8**, 14485 (2017).

66. Lewis, R.M.R. *Guide to Graph Colouring* (Springer International Publishing, 2021).

67. Cotler, J. & Wilczek, F. Quantum overlapping tomography. *Phys. Rev. Lett.* **124**, 100401 (2020).

68. Magnard, P. et al. Fast and unconditional all-microwave reset of a superconducting qubit. *Phys. Rev. Lett.* **121**, 060502 (2018).

69. Martinez, L. A., Rosen, Y. J. & DuBois, J. L. Improving qubit readout with hidden Markov models. *Phys. Rev. A* **102**, 062426 (2020).

70. Didier, N., Bourassa, J. & Blais, A. Fast quantum nondemolition readout by parametric modulation of longitudinal qubit-oscillator interaction. *Phys. Rev. Lett.* **115**, 203601 (2015).

71. Gross, D., Liu, Y.-K., Flammia, S. T., Becker, S. & Eisert, J. Quantum state tomography via compressed sensing. *Phys. Rev. Lett.* **105**, 150401 (2010).

72. Riofrío, C. A. et al. Experimental quantum compressed sensing for a seven-qubit system. *Nat. Commun.* **8**, 15305 (2017).

73. Postler, L. et al. Demonstration of fault-tolerant universal quantum gate operations. *Nature* **605**, 675 (2022).

74. Langford, N. K. Errors in quantum tomography: diagnosing systematic versus statistical errors. *New J. Phys.* **15**, 035003 (2013).

75. Temme, K. & Verstraete, F. Quantum chi-squared and goodness of fit testing. *J. Math. Phys.* **56**, 012202 (2015).

76. Parallel_QND_measurement_tomography; https://doi.org/10.5281/zenodo.7341393 (2022).

AUTHOR CONTRIBUTIONS

All authors contributed to the theoretical development of the proposed method. L.P. performed the experiments on the IBM quantum processor. All authors contributed to the discussion of the results and the writing of the article.

COMPETING INTERESTS

The authors declare no competing interests.

ADDITIONAL INFORMATION

Supplementary information The online version contains supplementary material available at https://doi.org/10.1038/s41534-023-00688-7.

Correspondence and requests for materials should be addressed to L. Pereira, J. J. García-Ripoll or T. Ramos.

Reprints and permission information is available at http://www.nature.com/reprints

Publisher's note Springer Nature remains neutral with regard to jurisdictional claims in published maps and institutional affiliations.